Check for updates

The Effect of Texture Floor Profile on the Lubricant Film Thickness in a Textured Hard-On-Soft Bearing With Relevance to Prosthetic Hip Implants

Quentin Allen
Department of Mechanical Engineering,
University of Utah,
1495 East 100 South (1550 MEK),
Salt Lake City, UT 84112
e-mail: q.s.allen@utah.edu

Bart Raeymaekers[1]
Department of Mechanical Engineering,
University of Utah,
1495 East 100 South (1550 MEK),
Salt Lake City, UT 84112
e-mail: bart.raeymaekers@utah.edu

Polyethylene wear debris limits the longevity of prosthetic hip implants. We design a pattern of axisymmetric texture features to increase hydrodynamic pressure and lubricant film thickness and, thus, reduce solid-on-solid contact, friction, and wear in hard-on-soft prosthetic hip implant bearings. Specifically, we study the effect of the texture floor profile on the lubricant film thickness using a soft elastohydrodynamic lubrication model. We compute the optimum texture parameters that maximize the lubricant film thickness for different texture floor profiles, as a function of bearing operating conditions. Flat texture floor profiles create thicker lubricant films than sloped or curved texture floor profiles for their respective optimum texture design parameters. We find that the texture feature volume is the most important parameter in terms of maximizing the lubricant film thickness, because a linear relationship exists between the texture feature volume with optimum texture parameters and the corresponding optimum lubricant film thickness, independent of the texture floor profile. [DOI: 10.1115/1.4047753]

Keywords: surface texture, elastohydrodynamic lubrication, numerical analysis, film thickness, artificial joints

1 Introduction

Total hip replacement (THR) is one of the most commonly performed surgeries in the United States (US). About 370,700 THR surgeries were performed in the US in 2014 (most recent publicly available data from the National Inpatient Sample), and the number of THR surgeries is projected to increase to 635,000 by 2030 [1]. THR surgery involves replacing the natural hip joint with a prosthetic hip implant, which typically comprises a femoral stem that is fixed in the femur bone and attached to a femoral head that articulates with an acetabular liner/cup implanted in the pelvis (see Ref. [2] for figures and detailed information about THR). The bearing between the femoral head and the acetabular liner/cup replaces the natural hip function. Different material pairs for prosthetic hip implant bearing surfaces exist, including metal-on-polyethylene (MoP), metal-on-metal (MoM), ceramic-on-polyethylene (CoP), and ceramic-on-ceramic (CoC). The hard-on-soft (MoP, CoP) material combinations account for more than 90% of the new prosthetic hip implants in the US in 2014 [3]. Evans et al. reviewed multiple case studies and national registries and estimate that historically, 89% of prosthetic hip implants achieve 15 years of useful life, 70% last 20 years, and 58% reach 25 years before failing [4].

A revision surgery replaces a failed implant with a new one, which is costly for the healthcare system and risky for the patient. The most common failure modes of prosthetic hip implants include mechanical loosening (55%), instability (14%), and osteolysis around an otherwise well-fixed implant (13%) [5]. Osteolysis is the weakening and loss of bone due to the body's inflammatory response to foreign material originating from the prosthetic hip implant, typically because of wear. Osteolysis often results in implant loosening and instability, and has been linked to polyethylene wear debris [6]. Hence, reducing polyethylene wear remains important to increasing the longevity of hard-on-soft prosthetic hip implants, in particular because the average age of THR patients decreases, while their life expectancy increases, thus making revision surgery more likely [7].

Methods to reduce polyethylene wear can be categorized into either improving the mechanical properties of the polyethylene material or altering the design of the bearing surfaces. The introduction of highly cross-linked (HXL) ultra-high molecular weight polyethylene (UHMWPE) has decreased polyethylene wear both in vitro [8] and in vivo [9]. Furthermore, infusing or blending HXL polyethylene with vitamin-E further reduces wear by increasing oxidation resistance [10,11]. Alternatively, advanced ceramic materials increase the hardness and wettability and decrease surface roughness of the femoral heads, thereby also reducing polyethylene wear [12]. Similarly, surface coatings such as diamond-like carbon [13,14], tantalum [15], or titanium nitride [16] increase hardness and reduce surface roughness of the femoral head to reduce polyethylene wear.

Several research groups have used experiments and simulations to demonstrate that texturing one of the bearing surfaces can reduce friction and wear by creating lubricant reservoirs [17], trapping wear particles [18], or increasing hydrodynamic pressure in the fluid lubricant film between the bearing surfaces, which increases the lubricant film thickness under constant bearing load. Many papers use surface texturing to reduce friction and wear in a variety of engineering applications [19,20]. However, in this paper, we focus only on textured hard-on-soft prosthetic hip implant bearings that use the latter mechanism to reduce polyethylene wear.

Different types of experiments have been performed. For instance, Ito et al. used a hip joint simulator, which allows simulating in vivo gait and loading, to show that using a textured compared to a smooth CoCrMo femoral head with an UHMWPE liner reduces the friction coefficient and UHMWPE wear [17]. In contrast, pin-on-disk (PoD) experiments employ simplified kinematics,

[1]Corresponding author.
Contributed by the Tribology Division of ASME for publication in the JOURNAL OF TRIBOLOGY. Manuscript received April 8, 2020; final manuscript received June 29, 2020; published online August 3, 2020. Assoc. Editor: Xiaolei Wang.

 Copyright © 2020 by ASME

Downloaded from http://asmedigitalcollection.asme.org/tribology/article-pdf/143/2/021801/6555147/trib_143_2_021801.pdf by Bart Raeymaekers on 25 August 2020

loading, and contact geometry consisting of a pin articulating with a disk, to enable faster wear measurements of material pairs than a hip joint simulator experiment. For instance, Borjali et al. [21,22] and Langhorn et al. [23] used PoD experiments with a polyethylene pin and CoCrMo disk and show that depending on the texture geometry, a pattern of shallow texture features on the CoCrMo disk can reduce polyethylene wear by 50% compared to a smooth disk, due to increased lubricant film thickness between the bearing surfaces. Furthermore, Chyr et al. [24] and Qiu et al. [25] used a hybrid apparatus that combines the speed of PoD experiments with operating conditions more closely related to in vivo gait, and experimentally showed that CoCrMo cylinders with shallow texture features reduce the friction coefficient by up to 50% compared to smooth cylinders, depending on the texture geometry and operating conditions. Other experimental configurations include ring-on-disk (RoD) where a ring spins above a stationary disk [26], and ball-on-disk (BoD) where a ball and a disk articulate with a combination of sliding and rolling [27].

Experimental works have also attempted to quantify the influence of specific texture design parameters, including texture aspect ratio, texture density, texture shape, and texture floor profile, on different lubrication metrics such as lubricant film pressure and thickness, friction coefficient, and wear of the bearing surfaces. Here, we define the texture aspect ratio and density as the ratio of the depth and characteristic diameter of the texture feature, and the ratio of the bearing surface area covered by texture features and the total bearing area, respectively [24]. The texture shape defines the two-dimensional (2D) perimeter of the texture feature on the bearing surface, whereas the texture floor profile specifically describes the three-dimensional (3D) geometry of the texture feature floor (local depth), which can be flat, sloped, or curved. Furthermore, we refer to specific bearing parameters, such as the relative velocity between bearing surfaces, lubricant properties, and the externally applied load or bearing load-carrying capacity, as the bearing operating conditions.

Several researchers experimentally determined the texture aspect ratio and density required to increase the lubricant film thickness [28,29] and decrease the friction coefficient and wear [30,31] compared to smooth bearing surfaces. For instance, Cho and Choi performed PoD experiments of UHMWPE pins articulating with textured steel disks to show that the friction coefficient decreases with increasing texture density and decreasing texture aspect ratio [32]. Zhang et al. used RoD experiments of textured stainless steel and smooth UHMWPE, and smooth stainless steel and textured UHMWPE to find the optimum texture densities that minimize the friction coefficient in both texturing configurations [33]. A few other studies experimentally showed that altering the texture shape, or re-orienting it with respect to the lubricant flow direction, can also increase the lubricant film thickness [34] and decrease the friction force [35,36] for both unidirectional and reciprocating sliding. The pattern of the texture features also affects the friction coefficient [37], including combining multiple shapes of texture features [38], or only texturing the bearing inlet, see, e.g., Ref. [39]. Note that there is no defined bearing inlet on the femoral head of a prosthetic hip implant because the direction of motion constantly changes, thus eliminating the potential benefits of partial texturing for this application.

Numerical simulations have also been used to determine optimum texture design parameters that maximize lubricant film thickness and minimize friction and wear, see e.g., [40,41]. Hydrodynamic lubrication (HL) models solve the Navier–Stokes or Reynolds equations to compute the lubricant film pressure between a textured and smooth bearing surface in relative motion [42,43]. Elastohydrodynamic lubrication (EHL) models additionally solve the elastic equations to compute the deformation of the bearing surfaces in conjunction with the lubricant film pressure [44]. EHL models are commonly used for textured MoM prosthetic hip implant bearing surfaces because metallic materials are easily modeled as linear elastic [45,46]. Soft EHL models work when one or both of the bearing surfaces deform at low pressure [47]. Qiu et al. used a soft EHL model of textured CoCrMo and smooth UHMWPE to determine the optimum texture parameters for a specific operating condition of prosthetic knee implants and found that they compared closely to naturally occurring texture parameters on human articular cartilage [25]. Allen and Raeymaekers also employed a soft EHL model to study textured CoCrMo and smooth UHMWPE and compute optimum texture design parameters for a wide range of bearing operating conditions [48]. Furthermore, simulations of different texture shapes showed that the orientation of non-axisymmetric shapes with respect to the lubricant flow direction changes the lubricant film pressure and bearing load-carrying capacity [49,50], and the friction force [51,52]. Other publications document bearings that comprise a textured UHMWPE and a smooth metal surface [53,54], and found similar lubricant film thickness and bearing load-carrying capacity results to those obtained for a bearing with a smooth UHMWPE and textured metal surface. However, texturing the UHMWPE surface may result in a changing texture geometry as the UHMWPE surface wears under contact, thus altering the texture geometry and potentially changing the properties of the bearing.

Experiments and simulations also point to the effect of the texture floor profile on the lubricant film pressure and thickness. Shen and Khonsari measured the lubricant film pressure of textured, oil-lubricated steel contacts in RoD experiments and found that texture features with a flat compared to sloped texture floor profile result in higher bearing load-carrying capacity [55]. Lu et al. showed that non-axisymmetric texture shapes and texture floor profiles result in directional friction coefficients with PoD experiments of steel contacts lubricated with oil [56]. Nanbu et al. performed EHL simulations of oil-lubricated steel surfaces with grooves to optimize the floor profile and found that a sudden change of the texture depth, i.e., a step bearing, at the texture inlet and gradual change in texture depth, i.e., a wedge bearing, at the texture outlet maximize lubricant film pressure under unidirectional sliding [57]. Several HL simulations also optimized the texture floor profiles under unidirectional sliding and show that texture floor profiles oriented with respect to the lubricant flow direction such that a step bearing occurs at the texture inlet and a wedge bearing at the texture outlet maximizes the lubricant film thickness, lubricant film pressure, and bearing load-carrying capacity [58–60].

The literature documents optimizing non-axisymmetric texture shapes and texture floor profiles to maximize lubricant film pressure and lubricant film thickness for unidirectional and reciprocating sliding. In contrast, multidirectional sliding, which occurs in prosthetic hip implants, requires axisymmetric texture shapes and floor profiles because the sliding motion constantly changes direction in the ball-in-socket design. However, no publications document optimizing the texture floor profile of axisymmetric surface texture shapes for multidirectional sliding, specifically in the context of increasing the lubricant film thickness in hard-on-soft prosthetic hip implant bearings. Thus, the objective of this paper is to determine the effect of the texture floor profile and texture design parameters of axisymmetric surface texture features, on the lubricant film thickness in textured hard-on-soft bearings, for a range of operating conditions relevant to prosthetic hip implants.

2 Methods

We model a rigid CoCrMo surface with an array of five axisymmetric texture features sliding parallel to a deformable polyethylene counterface with velocity U, thus representing a small portion of an MoP prosthetic hip implant bearing. Five texture features are required to obtain results free from edge effects. Increasing the number of texture features changed the average lubricant film pressure result by less than 3.5%. Figure 1 shows a schematic of the model before (solid line, bearing spacing c) and after polyethylene deformation $d(x,y)$ (dashed line, lubricant film thickness $h(x,y) = c + d(x,y)$). Each texture feature has a constant radius $r_p = 50\ \mu$m, depth

Downloaded from http://asmedigitalcollection.asme.org/tribology/article-pdf/143/2/021801/6555147/trib_143_2_021801.pdf by Bart Raeymaekers on 25 August 2020

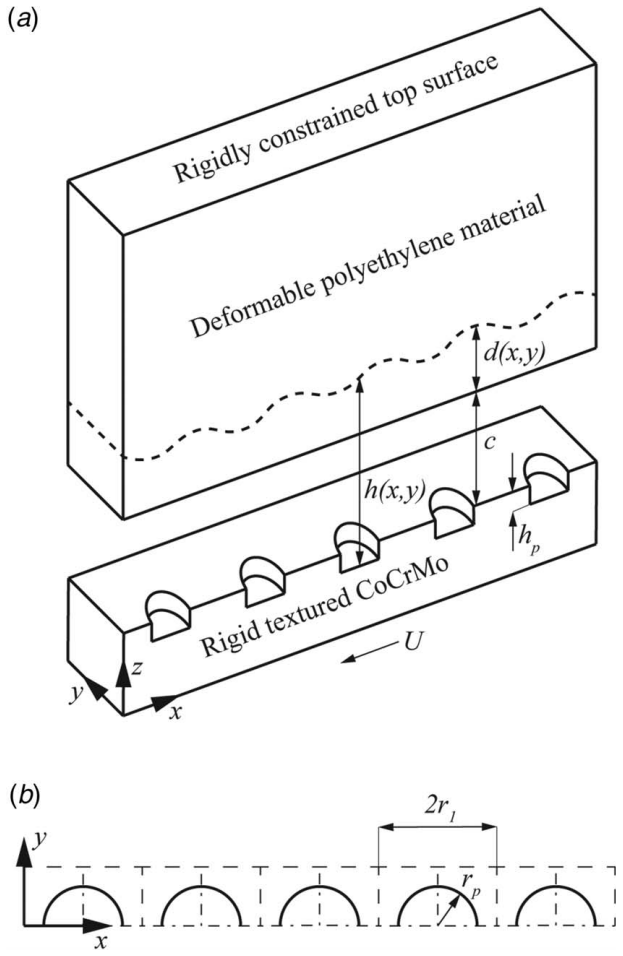

Fig. 1 (*a*) Schematic of the EHL model, showing the array of texture features (only half is modeled because of symmetry). The polyethylene deformation is schematically illustrated with a dashed line. (*b*) Top view of the textured surface.

h_p, and is enclosed within an imaginary square cell of length $2r_1$ that defines the spacing between texture features. We neglect the curvature and eccentricity of a spherical prosthetic hip implant because we only consider a small section of the prosthetic hip implant bearing. The array of texture features is symmetric with respect to its centerline along the sliding direction, and thus, we apply symmetry boundary conditions to only simulate half of the array (Fig. 1). The texture aspect ratio and texture density, which we define as the ratio between the depth of the texture feature and the diameter of the circular texture outline on the rigid surface ($\epsilon = h_p/2r_p$), and the ratio between the textured area and the total surface area ($S_p = \pi r_p^2/4r_1^2$), respectively, define the geometry of the axisymmetric texture features.

We simultaneously solve the Reynolds equation to determine the lubricant film pressure and solve the elastic equations to compute the polyethylene deformation. The two-dimensional, steady-state, incompressible, iso-viscous Reynolds equation is given as

$$\frac{\partial}{\partial x}\left(h^3\frac{\partial p}{\partial x}\right)+\frac{\partial}{\partial y}\left(h^3\frac{\partial p}{\partial y}\right)=6\mu U\left(\frac{\partial h}{\partial x}\right) \tag{1}$$

where x and y represent Cartesian coordinates, $p(x,y)$ is the lubricant film pressure, $h(x,y)$ is the lubricant film thickness, μ is the dynamic viscosity of the lubricant, and U is the relative sliding velocity between the rigid CoCrMo and polyethylene bearing surfaces. We non-dimensionalize the Reynolds equation to render the results independent of the specific setup evaluated in this paper using the following non-dimensional parameters that have been established in previous works [25]: $X = x/r_p$, $Y = y/r_p$, $H(X,Y) = h(x,y)/c$, and $P(X,Y) = p(x,y)/p_0$. We also define a non-dimensional flow factor to describe the bearing operating conditions as $\lambda = 3\mu U/2r_p p_0$, and a non-dimensional bearing surface separation as $\delta = c/r_p$, where p_0 is the atmospheric pressure (101,325 Pa) and c is the dimensional bearing surface separation. The non-dimensional Reynolds equation is given as

$$\frac{\partial}{\partial X}\left(H^3\frac{\partial P}{\partial X}\right)+\frac{\partial}{\partial Y}\left(H^3\frac{\partial P}{\partial Y}\right)=\frac{\lambda}{\delta^2}\left(\frac{\partial H}{\partial X}\right) \tag{2}$$

We solve Eq. (2) using the finite difference method (FDM) with central discretization and a grid size of 301×301 nodes per imaginary cell around each texture feature. The inlet and the outlet of the array of five texture features remain at atmospheric pressure ($P(0,Y) = P(10r_1/r_p,Y) = 1$), and we impose symmetry boundary conditions ($\partial P/\partial Y(X,0) = \partial P/\partial Y(X,r_1/r_p) = 0$) on the other boundaries. Furthermore, we enforce the Reynolds cavitation condition at each iteration of the pressure computation ($P(X,Y) \geq P_{cav}$), similar to other simulations [53,58], and ensure the lubricant film pressure does not decrease below the vapor pressure of water (5,630 Pa). We iterate the pressure solution until the $L2$-norm, or Frobenius-norm [61], of the difference between consecutive iterations is less than 10^{-3}. A convergence study shows that increasing the number of nodes or enforcing a more stringent convergence criterion changes the results by less than 2%, while significantly increasing the computation time.

We apply the converged pressure solution as a boundary condition to the bottom surface of a finite element analysis (FEA) model of the polyethylene counterface. We use symmetry boundary conditions on all side surfaces of the polyethylene, including the inlet and outlet sides, and we rigidly fix the top surface to represent a small portion in the center of the polyethylene acetabular liner. The FEA model is not free to rotate, and therefore, the effect of lubricant shear forces on the lubricant film thickness is negligible compared to that of the lubricant film pressure. We use a mesh of 20 quadratic hexahedral elements across each imaginary cell around a texture feature and 40 elements to model the (3 mm) thickness of the acetabular liner. Mesh convergence studies show that increasing the number of elements changes the results by less than 0.5%. We model the polyethylene material using a linear elastic constitutive model of UHMWPE with Young's modulus $E = 0.9$ GPa and Poisson's ratio $\nu = 0.46$ [62].

The FEA (ANSYS) solves the deformation of a linear elastic, isotropic material as $\sigma = Ce$, where σ is the Cauchy stress tensor, C is the stiffness tensor, and e is the strain tensor. The linear elastic constitutive model is accurate for the deformation resulting from pressure values less than approximately 10 MPa, documented in similar soft EHL problems [63]. The maximum pressure observed in this work did not exceed 4.5 MPa. We add the polyethylene deformation to the bearing surface separation c to update the lubricant film thickness and recalculate the lubricant film pressure. We iterate between the lubricant film pressure and polyethylene deformation solutions until the $L2$-norm of the difference between consecutive deformation iterations changes by less than 10^{-3}. We compute the bearing load-carrying capacity from the absolute pressure in the lubricant film, $W = \int\int P(X,Y)dXdY = P_{avg}$, and compare this result with the external pressure load applied to the bearing. Note that $W = 1$ indicates no load-carrying capacity. We adjust the bearing surface separation until the lubricant film pressure, polyethylene deformation, and bearing load-carrying capacity all simultaneously converge, and the bearing load-carrying capacity is within 5% of the external pressure load. Figure 2 shows a flowchart of the numerical simulation.

We perform the simulations on a desktop computer with four cores. Runtimes to reach a converged solution ranged between 17.5 min and 3.5 days, with an average runtime of 3.3 h (solving the Reynolds and elastic equations 16 times on average).

We simulate texture features with different axisymmetric texture floor profiles including spherical (curved), cylindrical (flat), and

Downloaded from http://asmedigitalcollection.asme.org/tribology/article-pdf/143/2/021801/6555147/trib_143_2_021801.pdf by Bart Raeymaekers on 25 August 2020

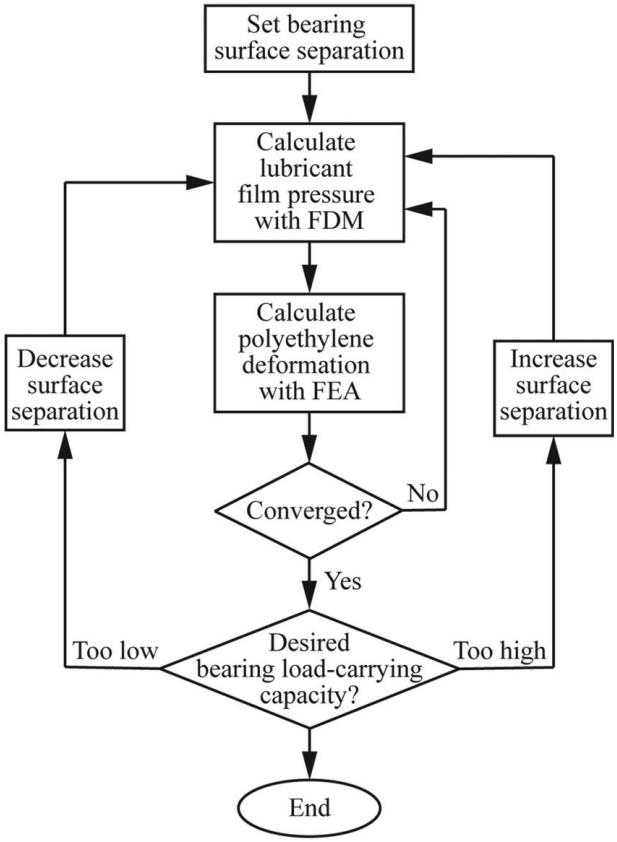

Fig. 2 Flowchart of the numerical simulation

conical (sloped), to determine the effect of texture floor profile on the lubricant film thickness. Figure 3 shows a schematic of axisymmetric texture features with the different texture floor profiles. Note that in theory, dH/dX will be infinite at the edge of the cylindrical texture features. However, the mesh required for the finite difference method results in a finite value of the derivative that allows us to solve Eq. (2) for the cylindrical texture features.

Table 1 shows the ranges of the non-dimensional parameters we consider in the simulations. We specify a nominal value of each parameter, which we use whenever the parameter is held constant. We select the nominal values for numerical stability and meaningful comparisons across different bearing operating conditions. We simulate a non-dimensional bearing load-carrying capacity of up to 19.738, which corresponds to a dimensional value of 2 MPa, and is the bearing load-carrying capacity recommended for physical testing of hard-on-soft prosthetic hip implant materials [64]. We simulate the flow factor over several orders of magnitude, which exceeds the flow factor expected for a prosthetic hip implant but is necessary to maintain full-film lubrication in the EHL model and avoid contact between the bearing surfaces. Furthermore, we evaluate the texture density over its entire range, with $S_{p,max} = \pi/4$, and consider a range of texture aspect ratios that contains the optimum value to maximize the lubricant film thickness [48].

The minimum lubricant film thickness for each set of bearing operating conditions and texture design parameters allows

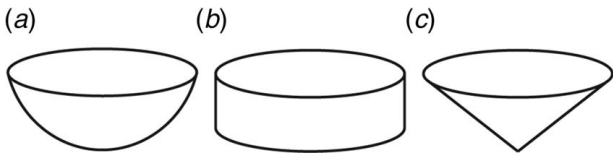

Fig. 3 Axisymmetric texture features with different texture floor profiles: (a) spherical, (b) cylindrical, and (c) conical

Table 1 Non-dimensional parameters

Parameter	Minimum value	Maximum value	Nominal value
Bearing load-carrying capacity, W	2.467	19.738	4.935
Flow factor, λ	0.003	0.300	0.300
Texture aspect ratio, ϵ	0.010	0.100	0.050
Texture density, S_p	0.100	0.700	0.200

evaluating the effect of the surface texture on the lubricant film thickness because it describes where the bearing surfaces first make contact. Thus, we determine the texture parameters that result in the largest value of the minimum lubricant film thickness and refer to them as the optimum texture parameters (ϵ_{opt} and $S_{p\ opt}$). Correspondingly, we define the optimum lubricant film thickness H_{opt} as the largest attainable value of the non-dimensional minimum lubricant film thickness for a specific set of bearing operating conditions, resulting from the optimum texture parameters (ϵ_{opt} and $S_{p\ opt}$).

3 Results and Discussion

3.1 Typical Elastohydrodynamic Lubrication Solutions. The shape and floor profile of the texture features affect the local lubricant film pressure, because they affect the local lubricant velocity. Figure 4(*a*) shows a 3D view of the non-dimensional lubricant film pressure across the array of spherical texture features, for typical texture parameters ($\epsilon = 0.05$ and $S_p = 0.20$) and bearing operating conditions ($W = 4.935$ and $\lambda = 0.300$). Figure 4(*b*) shows a 3D view of the non-dimensional lubricant film thickness across the array. Furthermore, Fig. 4(*c*) shows the non-dimensional lubricant film pressure and Fig. 4(*d*) shows the non-dimensional lubricant film thickness at the centerline of the middle texture feature in the array and for each of the three texture floor profiles considered in this work. We report the lubricant film thickness and polyethylene deformation non-dimensionalized with the texture feature diameter ($2r_p = 100\ \mu$m), as this remains constant throughout the entire paper. Thus, $H(X,Y) = h(x,y)/2r_p$, $D(X,Y) = d(x,y)/2r_p$. This contrasts with the bearing surface separation c, used for the non-dimensional lubricant film thickness in Eq. (2), which changes in each simulation. Figure 4(*e*) shows the local average lubricant velocity, averaged across the lubricant film thickness and non-dimensionalized with the average lubricant velocity at the inlet of the array of texture features, and Fig. 4(*f*) shows the derivative of the non-dimensional average lubricant velocity along the centerline of the middle texture feature in the array.

From Fig. 4, we observe that the non-dimensional lubricant film pressure decreases to the cavitation pressure at the texture inlet because the non-dimensional average lubricant velocity decreases as the lubricant enters a diverging channel. Within the cylindrical texture features, the non-dimensional lubricant film pressure then increases linearly and abruptly reaches a maximum at the outlet of the texture feature. This maximum becomes more pronounced with increasing texture aspect ratio because the lubricant volume that exits the step bearing at the texture outlet increases linearly with the texture aspect ratio. In the case of spherical and conical texture features, the non-dimensional lubricant film pressure changes nonlinearly within the texture feature and does not experience an abrupt increase at the outlet of the texture feature because, in contrast with the cylindrical texture feature, a smoother transition exists from the texture feature to the untextured bearing area (wedge bearing). Nanbu et al. [57] and Brizmer et al. [65] showed similar lubricant film pressure as in Fig. 4.

The non-dimensional average lubricant velocity along the centerline of the texture feature is inversely proportional to the non-dimensional lubricant film thickness because the local lubricant

Downloaded from http://asmedigitalcollection.asme.org/tribology/article-pdf/143/2/021801/6555147/trib_143_2_021801.pdf by Bart Raeymaekers on 25 August 2020

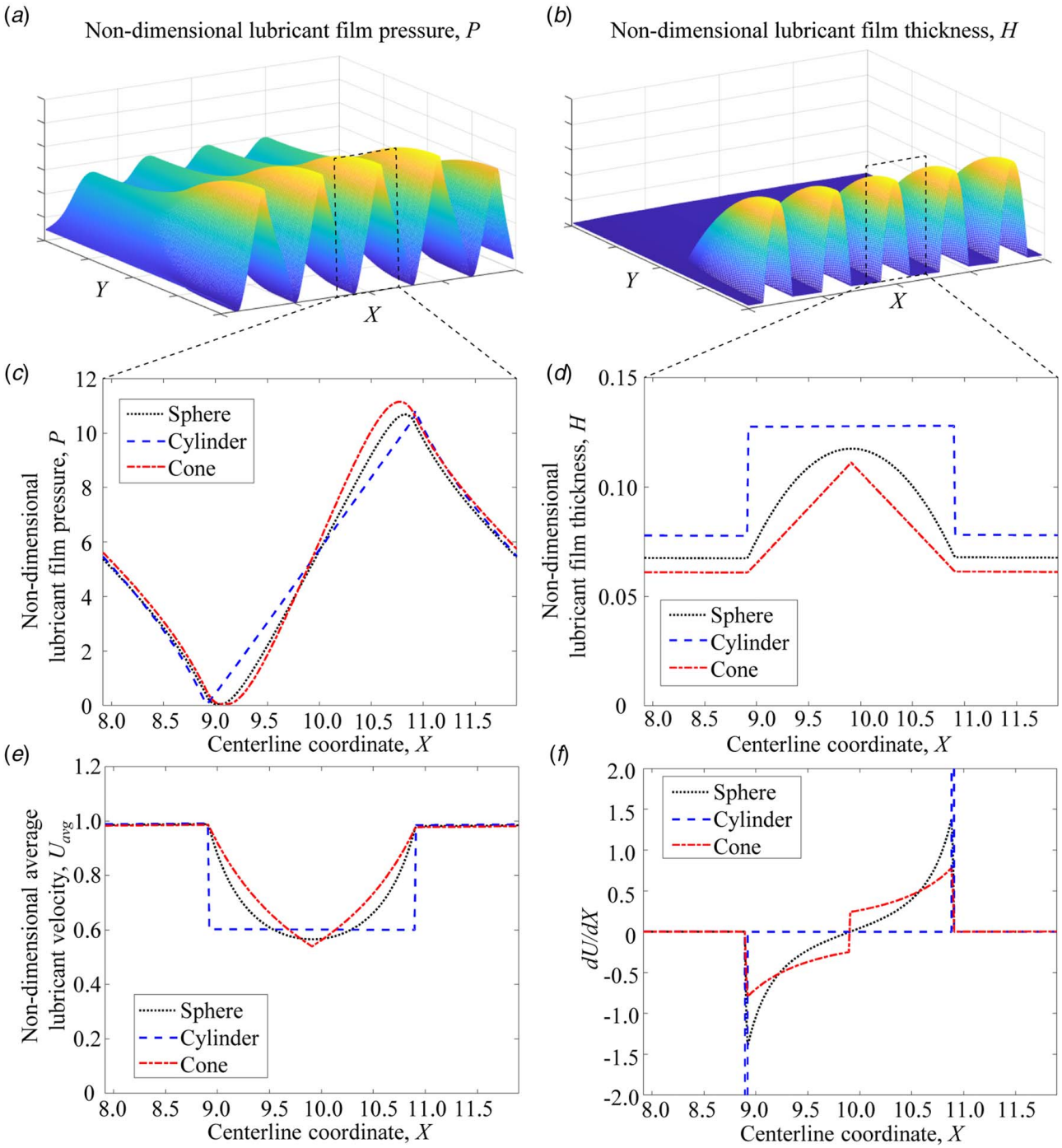

Fig. 4 (*a*) 3D view of the non-dimensional lubricant film pressure for an array of texture features with spherical texture floor profiles ($\epsilon = 0.050$, $S_p = 0.200$, $W = 4.935$, and $\lambda = 0.300$); (*b*) 3D view of the lubricant film thickness for the array of texture features; (*c*) non-dimensional lubricant film pressure along the centerline of the middle texture feature in the array; (*d*) non-dimensional lubricant film thickness; (*e*) non-dimensional average lubricant velocity, and (*f*) derivative of the non-dimensional average lubricant velocity

velocity decreases with increasing local lubricant film thickness to maintain a constant volumetric flowrate. The derivative of the non-dimensional average lubricant velocity with respect to the X-coordinate shows how the non-dimensional average lubricant velocity changes across the texture feature. A negative derivative indicates that the non-dimensional average lubricant velocity decreases, which corresponds to a diverging channel created by the texture floor profile. Likewise, a positive derivative corresponds to a converging channel. Thus, we observe that the non-dimensional average lubricant velocity decrease caused by the divergent floor profile of the cylindrical texture feature is localized at the texture inlet, and the non-dimensional average lubricant velocity increase caused by the convergent texture floor profile is localized at the texture outlet. A region of constant non-dimensional average lubricant velocity exists inside the cylindrical texture feature, which corresponds to the region of linearly increasing non-dimensional lubricant film pressure. In contrast, the spherical and conical texture floor profiles show decreasing non-dimensional average lubricant velocity (and diverging flow) throughout the entire front half of the texture feature, and increasing non-dimensional

Downloaded from http://asmedigitalcollection.asme.org/tribology/article-pdf/143/2/021801/6555147/trib_143_2_021801.pdf by Bart Raeymaekers on 25 August 2020

average lubricant velocity (and converging flow) throughout the entire back half of the texture feature. This constantly changing non-dimensional average lubricant velocity explains the non-linear increase in non-dimensional lubricant film pressure observed inside the spherical and conical texture features.

The EHL solution accounts for the deformation of the soft polyethylene bearing surface. Figure 5(*a*) shows the polyethylene deformation and FEA model mesh, whereas Fig. 5(*b*) depicts the polyethylene deformation along the centerline of the middle texture feature in the array, for typical texture parameters ($\epsilon = 0.05$ and $S_p = 0.20$) and bearing operating conditions ($W = 4.935$ and $\lambda = 0.300$). From Fig. 5, we observe that the polyethylene deformation is approximately two orders of magnitude smaller than the lubricant film thickness, which explains why the texture feature geometry dominates the lubricant film thickness shown in Figs. 4(*b*) and 4(*d*).

3.2 Effect of Bearing Operating Conditions on Lubricant Film Thickness. Figure 6 shows the non-dimensional minimum lubricant film thickness as a function of texture aspect ratio for different values of the texture density, and for spherical (Figs. 6(*a*) and 6(*b*)), cylindrical (Figs. 6(*c*) and 6(*d*)), and conical (Figs. 6(*e*) and 6(*f*)) texture floor profiles. Furthermore, we present the results for constant bearing load-carrying capacity ($W = 4.935$) and varying flow factor λ (Figs. 6(*a*), 6(*c*), and 6(*e*)), and constant flow factor ($\lambda = 0.300$) and varying bearing load-carrying capacity W (Figs. 6(*b*), 6(*d*), and 6(*f*)). From Fig. 6, we observe that an optimum texture aspect ratio and texture density exist that maximize the non-dimensional minimum lubricant film thickness for each texture floor profile, and each set of operating conditions (W and λ). From Fig. 6, we observe that the minimum lubricant film thickness is less sensitive to the texture density than to the texture aspect ratio, as multiple lines overlap near the optimum, indicating that a range of texture density values (approximately $S_p = 0.10$–0.40) will maximize the non-dimensional minimum lubricant film thickness. Additionally, the non-dimensional minimum lubricant film thickness strongly depends on the texture aspect ratio for cylindrical texture features, indicated by lines with significant curvature where an obvious maximum exists in Figs. 6(*c*) and 6(*d*). The non-dimensional minimum lubricant film thickness with conical texture features does not depend significantly on the texture aspect ratio, as the value of the non-dimensional minimum lubricant film thickness remains almost constant with increasing texture aspect ratio as shown in Figs. 6(*e*) and 6(*f*). This is because a change in texture aspect ratio produces a greater change in texture feature volume for the cylindrical texture features than the conical and spherical texture features. Correspondingly, the optimum texture aspect ratio is higher for the conical than for the cylindrical texture features, under constant bearing operating conditions, because the conical texture features require a greater aspect ratio than the cylindrical ones to obtain a similar texture feature volume.

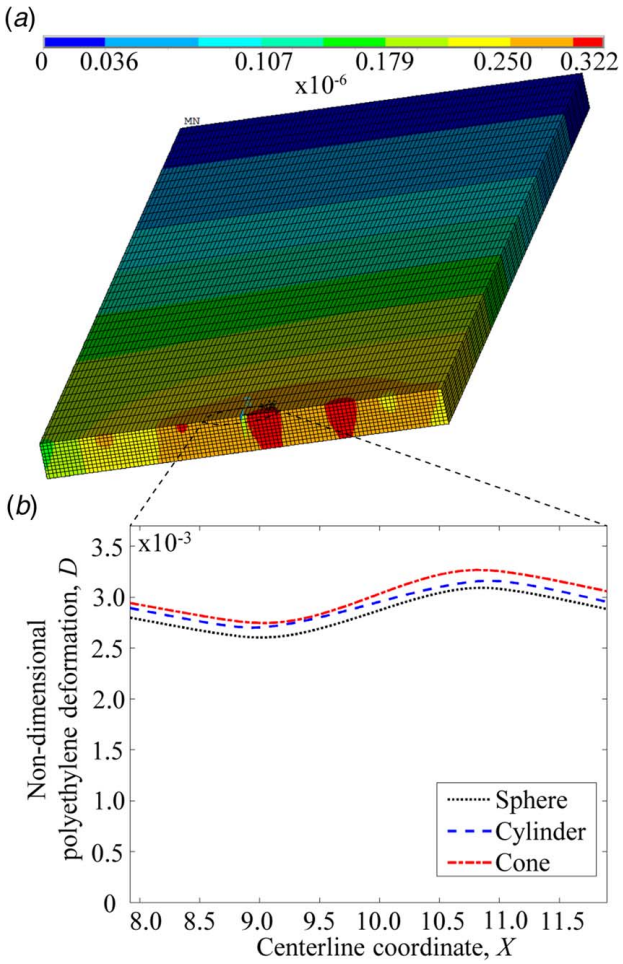

Fig. 5 (*a*) FEA model showing the polyethylene deformation results; (*b*) the non-dimensional polyethylene deformation at the centerline of the middle texture feature for spherical, cylindrical, and conical texture floor profiles

For the ease of discussion and nomenclature, we define the maximum value of the non-dimensional minimum lubricant film thickness obtained for each set of bearing operating conditions, and the corresponding texture aspect ratio and texture density, as the optimum lubricant film thickness and optimum texture parameters, respectively. Therefore, the optimum lubricant film thickness represents the best-case minimum lubricant film thickness for the given bearing operating conditions. Figure 7 shows the optimum lubricant film thickness as a function of (*a*) the flow factor with constant bearing load-carrying capacity ($W = 4.935$), and (*b*) the bearing load-carrying capacity with constant flow factor ($\lambda = 0.300$), for each texture floor profile, extracted from Fig. 6. We observe that the cylindrical and conical texture features create the thickest and thinnest lubricant films, respectively, differing approximately 11–15%. This is in agreement with the experimental results documented by Shen on Khonsari, who found that flat texture floor profiles create higher load-carrying capacity than sloped texture floor profiles [55]. It is not surprising that the cylindrical texture features produce the greatest lubricant film thickness because step bearings have long been known to be the optimum shape for increasing the load-carrying capacity [66]. We also observe that the optimum lubricant film thickness increases with increasing flow factor because it increases the lubricant viscosity and/or relative flow velocity. Furthermore, the optimum lubricant film thickness decreases with increasing bearing load-carrying capacity because the bearing surfaces are forced closer together as a result of the increasing external load.

To understand the results, we find mathematical best-fit equations to the data that minimize the least squares error. Best-fit equations for the optimum lubricant film thickness are power laws of the form $H_{opt} = a\lambda^b$ and $H_{opt} = aW^b$ for the flow factor and bearing load-carrying capacity, respectively, and appear as dotted lines in Fig. 7. The power law form of the best-fit equations arises from the Reynolds equation where the lubricant film thickness is raised to the third power while the lubricant film pressure and flow factor are not. The coefficient a represents the magnitude of the optimum lubricant film thickness at a unit flow factor or bearing load-carrying capacity, whereas the exponent b describes the effect of the bearing operating conditions. Tables 2 and 3 list a and b for the best-fit equations of the three texture floor profiles, as well as the R^2 values to describe the goodness-of-fit.

3.3 Optimum Texture Parameters as a Function of the Bearing Operating Conditions. Figure 8 shows the optimum

Downloaded from http://asmedigitalcollection.asme.org/tribology/article-pdf/143/2/021801/6555147/trib_143_2_021801.pdf by Bart Raeymaekers on 25 August 2020

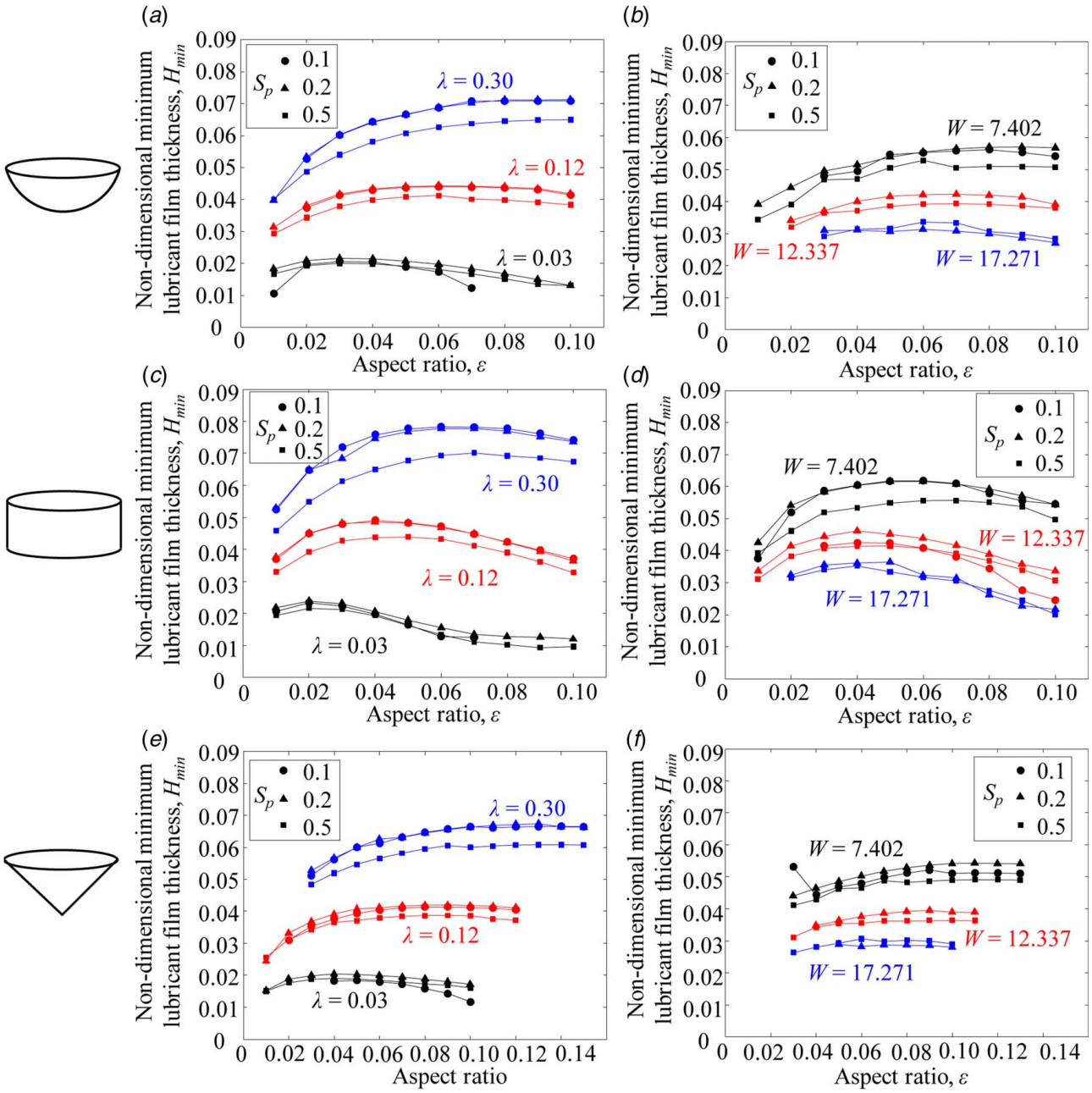

Fig. 6 Non-dimensional lubricant film thickness as a function of texture parameters and operating conditions. Spherical texture features with (*a*) $W = 4.935$ and varying λ, and (*b*) $\lambda = 0.300$ and varying W. Cylindrical texture features with (c) $W = 4.935$ and varying λ, and (*d*) $\lambda = 0.300$ and varying W. Conical texture features with (e) $W = 4.935$ and varying λ, and (*f*) $\lambda = 0.300$ and varying W.

texture parameters as a function of the flow factor with constant bearing load-carrying capacity ($W = 4.935$; Figs. 8(*a*) and 8(*b*)) and as a function of bearing load-carrying capacity with constant flow factor ($\lambda = 0.300$; Figs. 8(*c*) and 8(*d*)), for each texture floor profile. From Figs. 8(*b*) and 8(*d*), we observe that the optimum texture density increases with decreasing flow factor and increasing bearing load-carrying capacity. However, a texture density between $S_p = 0.10$–0.40 will result in a near-optimum film thickness for all cases considered in this work. This is in agreement with the experimental findings of Zhang et al. who found an optimum texture density between 0.10 and 0.30 for texture features on a stainless steel and UHMWPE surface, respectively [33]. From Figs. 8(*a*) and 8(*c*), we also observe that the optimum texture aspect ratio increases with increasing flow factor and decreasing bearing load-carrying capacity for all texture floor profiles, following the same trends as the optimum lubricant film thickness shown in Fig. 7.

We determine best-fit equations to predict the optimum texture aspect ratio as a function of flow factor and as a function of bearing load-carrying capacity and show them as dotted lines in Figs. 8(*a*) and 8(*c*), respectively. These equations take the form of a power law: $\epsilon_{opt} = a\lambda^b$, and $\epsilon_{opt} = aW^b$. Tables 4 and 5 list a and b for the best-fit equations of the three texture floor profiles, as well as the R^2 values to describe the goodness-of-fit.

Figure 8 determines the optimum texture aspect ratio as a function of flow factor (for constant $W = 4.935$) or as a function of bearing load-carrying capacity (for constant $\lambda = 0.300$). We perform multiple regression analysis to obtain equations for the optimum aspect ratio as a function of both bearing load-carrying capacity and flow factor. These equations take the form $\epsilon_{opt} = a\lambda^b W^c$, where a is a coefficient describing the optimum aspect ratio with unit flow factor and bearing load-carrying capacity, and b and c are exponents describing the effect of the flow factor and

Downloaded from http://asmedigitalcollection.asme.org/tribology/article-pdf/143/2/021801/6555147/trib_143_2_021801.pdf by Bart Raeymaekers on 25 August 2020

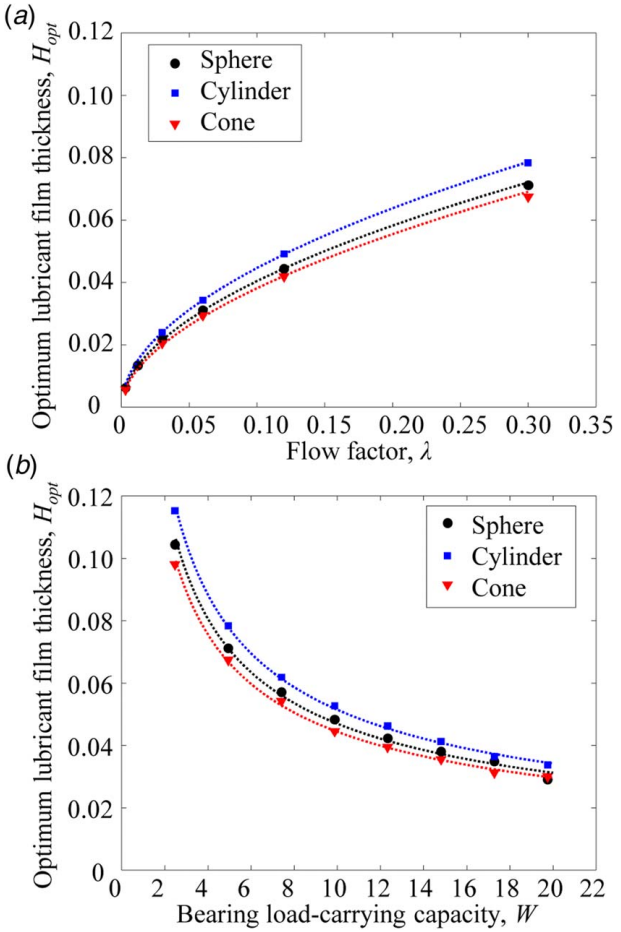

Fig. 7 Optimum lubricant film thickness for each texture floor profile as a function of (*a*) flow factor and (*b*) bearing load-carrying capacity

bearing load-carrying capacity, respectively. Table 6 lists a, b, and c for the multiple regression equations of the three texture floor profiles, as well as the R^2 values to describe the goodness-of-fit. Conical texture features require the largest coefficient a, indicating that the optimum aspect ratios are greater for conical texture features than for spherical and cylindrical texture features, as also apparent from Fig. 8.

3.4 Comparison of Texture Floor Profiles. We describe the different optimum texture aspect ratios for each texture floor profile in terms of texture feature volume. The volume of a cylindrical texture feature exceeds that of a spherical or conical one for a constant texture aspect ratio. Figure 9 shows the non-dimensional texture feature volume of the optimum texture parameters as a function of the flow factor with constant bearing load-carrying capacity ($W = 4.935$) (Fig. 9(*a*)) and as a function of the bearing load-carrying capacity with constant flow factor ($\lambda = 0.300$) (Fig. 9(*b*)). We non-dimensionalize the texture feature volume with πr_p^3, which corresponds to the volume of a cylindrical texture feature

Table 2 Parameters for the best-fit equations $H_{opt} = a\lambda^b$ for the data of Fig. 7(*a*)

	a	b	R^2
Sphere	0.1359	0.5269	0.9998
Cylinder	0.1462	0.5157	1.0000
Cone	0.1326	0.5418	0.9993

Table 3 Parameters for the best-fit equations $H_{opt} = aW^b$ for the data of Fig. 7(*b*)

	a	b	R^2
Sphere	0.1820	−0.5890	0.9926
Cylinder	0.1994	−0.5890	0.9984
Cone	0.1686	−0.5800	0.9979

with an aspect ratio of 0.5, i.e., the largest volume of an axisymmetric texture feature for a constant texture feature diameter. From Fig. 9, we observe that the cylindrical texture features contain the largest non-dimensional texture feature volume for each of the optimum texture parameters, with the smallest texture aspect ratio (Fig. 8). Tables 7 and 8 list a and b for the best-fit equations of $V_{opt} = a\lambda^b$ and $V_{opt} = aW^b$ for the three texture floor profiles, as well as the R^2 values to describe the goodness-of-fit. Note that the exponents b are nearly identical to those listed in Tables 4 and 5, indicating that the non-dimensional texture volume is directly related to the texture aspect ratio, and only the coefficient a changes between the best-fit equations for texture aspect ratio and non-dimensional texture feature volume. This is because the equation for volume of all the axisymmetric texture features depends on the depth, and the diameter of the texture features is accounted for with the non-dimensionalization. The best-fit equations are shown as dotted lines in Fig. 9.

Figure 10(*a*) shows the optimum texture aspect ratio as a function of the optimum lubricant film thickness for each texture floor profile. We observe that for each texture floor profile, a linear relationship exists between the optimum texture aspect ratio and the optimum lubricant film thickness; i.e., the best-fit equations are of the form $\epsilon_{opt} = aH_{opt} + b$. Table 9 lists the values of the slope, a, and intercept, b, along with the R^2 values for the best-fit equations illustrated as dotted lines in Fig. 10(*a*). We observe that the steepest and shallowest slopes exist for conical and cylindrical texture features, respectively. Thus, the conical texture features require a greater change of texture aspect ratio than the other texture features to initiate the same change of lubricant film thickness, because the shape of the conical texture features also requires a greater change of aspect ratio than the other texture features for the same change of texture feature volume. Other studies also demonstrate a linear relationship between the depth of texture features and the resulting lubricant film thickness [48,67]. We find the average ratio of optimum texture aspect ratio and optimum lubricant film thickness to be 1.51 for spherical texture features, 0.91 for cylindrical textures, and 2.25 for conical textures, closely related to the slopes of the best-fit lines listed in Table 9. Rahmani and Rahnejat performed 2D hydrodynamic lubrication simulations of textured bearings and found similar ratios of optimum texture feature depth and minimum lubricant film thickness in the range 0.80–0.85 for textures with flat floor profiles and 1.70–1.75 for texture features with triangular (sloped) floor profiles [68].

Figure 10(*b*) shows the non-dimensional optimum texture feature volume as a function of the optimum lubricant film thickness for all texture floor profiles. We observe that the results for all three axisymmetric texture floor profiles collapse on top of each other. Thus, a proportional linear relationship exists between the non-dimensional optimum texture feature volume and the optimum lubricant film thickness that holds true for axisymmetric texture features, independent of the texture floor profile. The best-fit equation to describe this linear relationship is $V_{opt} = 1.4073H_{opt} + 0.0073$, with $R^2 = 0.9180$. This best-fit equation is shown as a dotted line in Fig. 10(*b*). The texture feature volume determines the lubricant film pressure and bearing load-carrying capacity because the non-dimensional average lubricant velocity experiences a greater change with increasing texture feature volume for all texture floor profiles. The importance of texture feature volume as opposed to texture feature shape has also been shown previously for grooved piston liners lubricated with oil [69].

Downloaded from http://asmedigitalcollection.asme.org/tribology/article-pdf/143/2/021801/6555147/trib_143_2_021801.pdf by Bart Raeymaekers on 25 August 2020

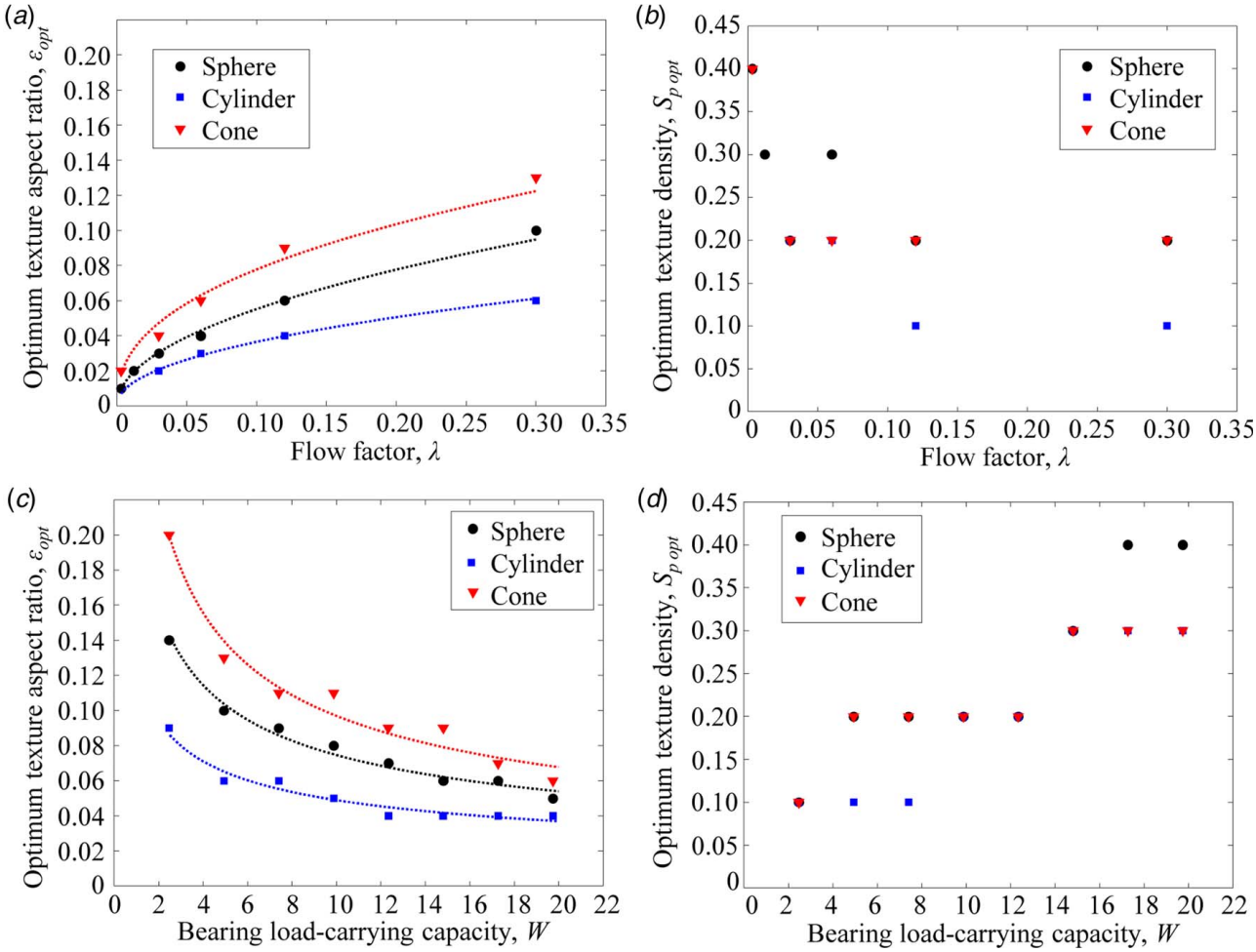

Fig. 8 (*a*) Optimum texture aspect ratio and (*b*) optimum texture density as a function of flow factor with constant $W = 4.935$. (*c*) Optimum texture aspect ratio and (*d*) optimum texture density as a function of bearing load-carrying capacity with constant $\lambda = 0.300$.

Understanding the relationship between the non-dimensional optimum texture feature volume and optimum lubricant film thickness for axisymmetric texture features enables computing the lubricant film thickness for axisymmetric texture floor profiles we have not specifically considered before in this work. For instance, we create an "inverse cone" axisymmetric texture feature with a step bearing or sudden floor profile drop along the outer diameter and a sloped gradual increase back to the center of the texture feature (Fig. 11(*a*)). Based on the results shown in Fig. 10(*b*), we determine that a non-dimensional texture feature volume of 0.078 achieves an optimum lubricant film thickness of 0.050, from which we calculate a texture aspect ratio of $\epsilon = 0.058$ for the inverse cone texture feature. Second, we choose an inverse cone texture aspect ratio of $\epsilon = 0.050$, which results in a non-dimensional texture feature volume of 0.067, from which we compute an optimum lubricant film thickness of 0.042. Figure 11(*b*) shows the non-dimensional minimum lubricant film thickness for selected simulations with the inverse cone texture floor profile with a texture density of $S_p = 0.20$. We indicate both calculations based on Fig. 10(*b*) with stars in Fig. 11(*b*). We observe that $\epsilon = 0.060$ optimizes the non-dimensional lubricant film thickness $H_{opt} = 0.050$ (computation 1) with $\lambda = 0.130$ and $W = 4.935$. We also observe that the optimum texture aspect ratio $\epsilon = 0.050$ results in an optimum lubricant film thickness $H_{opt} = 0.044$, which is very close to 0.042 (computation 2) with $\lambda = 0.100$ and $W = 4.935$. From Fig. 11(*b*), we observe that the optimum texture aspect ratio increases with increasing non-dimensional lubricant film thickness. Thus, the relationship between the non-dimensional optimum texture feature volume and optimum lubricant film thickness enables computing the optimum axisymmetric texture feature parameters for specific applications.

These results have implications for manufacturing of axisymmetric surface texture designs because they demonstrate that the texture feature volume is more important than the exact shape or floor profile. Laser surface texturing is commonly used to create a variety of surface texture designs [34,70]. Other methods such as micro-milling [30], indentation [71] or electrical/chemical etching

Table 4 Parameters for the best-fit curves of Fig. 8(*a*), $\epsilon_{opt} = a\lambda^b$

	a	b	R^2
Sphere	0.1715	0.4920	0.9972
Cylinder	0.1076	0.4699	0.9944
Cone	0.2011	0.4124	0.9777

Table 5 Parameters for the best-fit curves of Fig. 8(c), $\epsilon_{opt} = aW^b$

	a	b	R^2
Sphere	0.2184	−0.4660	0.9756
Cylinder	0.1248	−0.4070	0.9398
Cone	0.3183	−0.5160	0.9424

Downloaded from http://asmedigitalcollection.asme.org/tribology/article-pdf/143/2/021801/6555147/trib_143_2_021801.pdf by Bart Raeymaekers on 25 August 2020

Table 6 Parameters for the multiple regression equations to describe optimum texture aspect ratio as a function of both flow factor and bearing load-carrying capacity, $\epsilon_{opt} = a\lambda^b W^c$

	a	b	c	R^2
Sphere	0.3799	0.5114	−0.4449	0.9935
Cylinder	0.2193	0.4970	−0.3952	0.9726
Cone	0.4914	0.4405	−0.4827	0.9692

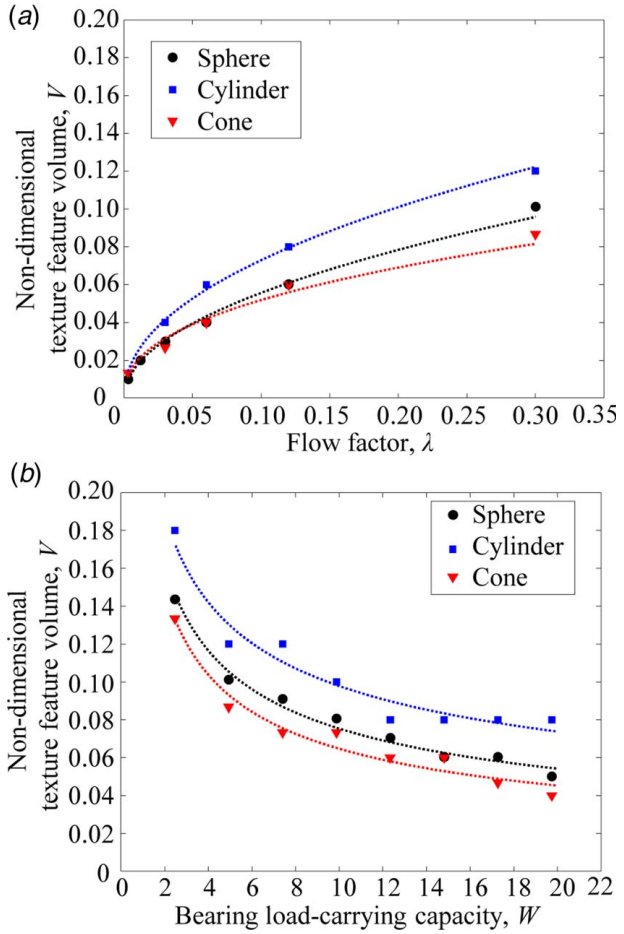

Fig. 9 Non-dimensional texture feature volume for the different texture floor profiles as a function of (*a*) flow factor with constant bearing load-carrying capacity ($W = 4.935$), and (*b*) bearing load-carrying capacity with constant flow factor ($\lambda = 0.300$)

Table 7 Parameters for the best-fit equations for non-dimensional texture feature volume of Fig. 9(*a*), $V_{opt} = a\lambda^b$

	a	b	R^2
Sphere	0.1736	0.4945	0.9969
Cylinder	0.2151	0.4699	0.9944
Cone	0.1341	0.4124	0.9777

Table 8 Parameters for the best-fit equations for non-dimensional texture feature volume of Fig. 9(*b*), $V_{opt} = aW^b$

	a	b	R^2
Sphere	0.2255	−0.4760	0.9769
Cylinder	0.2496	−0.4070	0.9398
Cone	0.2122	−0.5160	0.9424

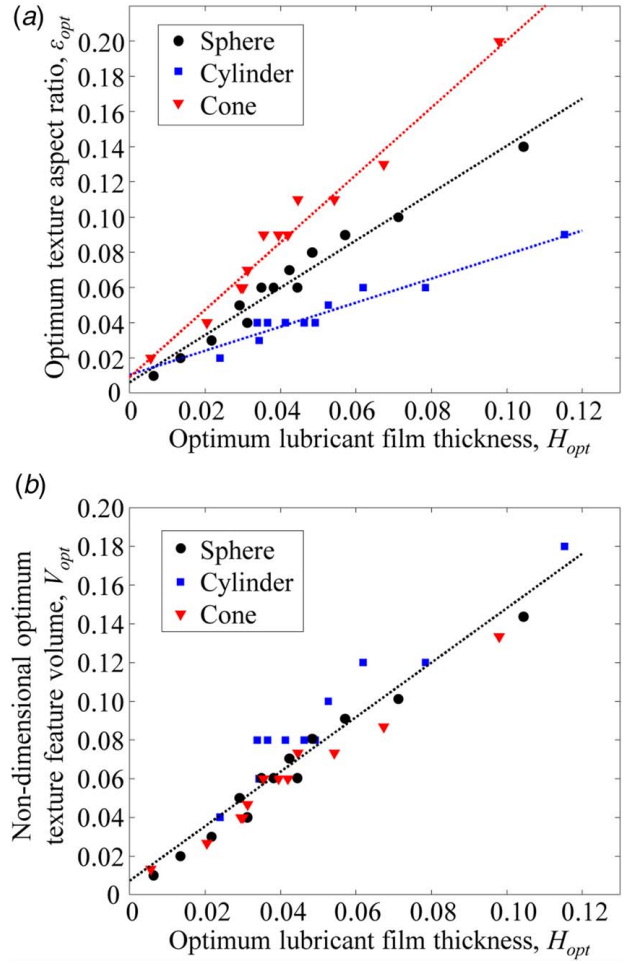

Fig. 10 (*a*) Optimum texture aspect ratio and (*b*) non-dimensional optimum texture feature volume as a function of the optimum lubricant film thickness

Table 9 Parameters for the best-fit equations, $\epsilon_{opt} = aH + b$ of Fig. 10(*a*)

	a	b	R^2
Sphere	1.3441	0.0061	0.9710
Cylinder	0.6826	0.0104	0.9324
Cone	1.9126	0.0092	0.9714

with photolithography masking [26,72] can also produce highly controlled patterns of surface texture features with various levels of flexibility. If the ideal cylindrical texture floor profile is unobtainable or prohibitively expensive with available manufacturing methods, one can at least replicate the optimum texture volume to achieve similar results.

3.5 Accuracy. The model we use in this work makes several assumptions. It is valid for full-film lubrication where the entire bearing load is carried by the lubricant film pressure and, thus, the bearing surfaces do not make contact. The smallest lubricant film thickness observed in our paper is comparable with the allowable average surface roughness of polyethylene acetabular

Downloaded from http://asmedigitalcollection.asme.org/tribology/article-pdf/143/2/021801/6555147/trib_143_2_021801.pdf by Bart Raeymaekers on 25 August 2020

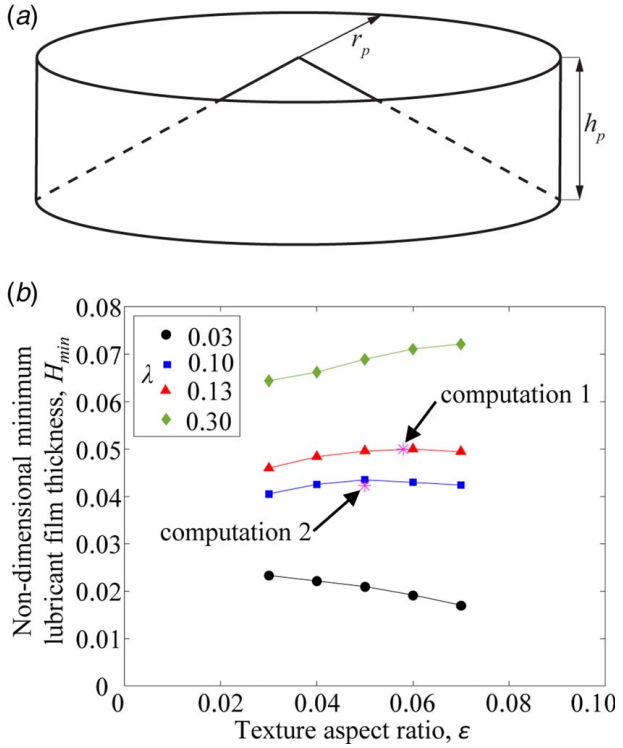

Fig. 11 (*a*) Schematic of the inverse cone texture feature; (*b*) non-dimensional minimum lubricant film thickness from the inverse cone texture feature as a function of texture aspect ratio, for different values of the flow factor (with $S_p = 0.20$ and $W = 4.935$), showing computations based on Fig. 10(*b*) as stars

liners and much larger than the allowable average surface roughness of metal and ceramic femoral heads, per ISO 7206-2 [73]. Others have shown that prosthetic hip implants operate in a full-film lubrication regime during the swing phase of the gait cycle [74,75]. Optimum texture features will maximize the lubricant film thickness during swing phase and help maintain full-film lubrication into a larger portion of the gait cycle than when no texture is present, to reduce friction and wear in prosthetic hip implants.

The assumptions inherent to the Reynolds equation (thin film, steady-state, laminar flow, isothermal, iso-viscous, and abundant lubricant supply) also apply to our model. We do not consider several phenomena that are known to occur in real prosthetic hip implants, such as lubricating protein contributions [76,77] or shear-thinning lubricant behavior [75]. We also employ a simplified cavitation model that is less accurate than more advanced mass-conserving algorithms [78–80]. Accounting for these phenomena will increase the accuracy of the lubricant film pressure and lubricant film thickness computations.

However, the intent of this paper is not to predict the exact value of the lubricant film pressure or thickness, but rather to evaluate how the different texture floor designs change the lubricant film thickness, relative to each other. Accounting for elastic deformation of the polyethylene surface affects the lubricant film pressure [53] and increases the bearing surface separation. We found that changing Young's modulus and Poisson's ratio of the polyethylene surface does not affect the optimum texture parameters. Ultimately, for the parameters evaluated in this paper, this results in a similar lubricant film thickness than those obtained from HL models of bearings in full-film lubrication. However, the surface deformation is important to understand the stress, strain, and wear of the bearing materials [48].

4 Conclusions

We conclude that the following:

(1) Under constant bearing operating conditions, the cylindrical texture features create the thickest lubricant film because the texture floor profile with a step bearing at the texture inlet and outlet leads to maximum and most abrupt change in the average lubricant velocity and, correspondingly higher local lubricant film pressure than the texture floor profiles with wedge bearings, where the average lubricant velocity changes gradually across the texture feature.
(2) We determine the optimum texture aspect ratio as a function of the bearing operating conditions for each texture floor profile. A proportional relationship exists between the optimum texture aspect ratio and the optimum lubricant film thickness. The proportionality constant varies with the texture floor profile, as conical microtexture features require a larger aspect ratio than a cylindrical texture feature to obtain the same texture feature volume.
(3) For the optimum texture parameters, the texture feature volume maintains a proportional relationship with the lubricant film thickness, independent of the texture floor profile, because the texture feature volume determines the lubricant film pressure and bearing load-carrying capacity.

Acknowledgment

This work was supported by the National Institutes of Health, National Institute of Arthritis and Musculoskeletal and Skin Diseases (Grant No. 1R03AR066826-01A1).

Data Availability

The data sets generated and supporting the findings of this article are obtainable from the corresponding author upon reasonable request. The authors attest that all data for this study are included in the paper. Data provided by a third party listed in Acknowledgement.

Nomenclature

c = nominal bearing surface separation, m
e = strain tensor
C = stiffness tensor
E = Young's modulus, Pa
U = relative sliding velocity between both bearing surfaces, m/s
V = non-dimensional texture feature volume
W = non-dimensional load-carrying capacity, $\int\int P(X,Y)\,dXdY = P_{avg}$
h_p = depth of texture feature, m
p_0 = atmospheric pressure, Pa
r_1 = half-length of imaginary square cell around each texture feature, m
r_p = radius of texture feature, m
D_{min} = minimum non-dimensional polyethylene deformation
H_{min} = minimum non-dimensional lubricant film thickness
H_{opt} = optimum non-dimensional lubricant film thickness
S_p = texture density, $\pi r_p^2/4r_1^2$
$S_{p\ max}$ = maximum texture density, $\pi/4$
$S_{p\ opt}$ = optimum texture density
V_{opt} = optimum non-dimensional texture feature volume
$d(x,y)$ = polyethylene deformation, m
$D(X,Y)$ = non-dimensional polyethylene deformation, $d/2r_p$
$h(x,y)$ = local lubricant film thickness, m
$H(X,Y)$ = non-dimensional local lubricant film thickness, h/c (simulation), or $h/2r_p$ (results)
$p(x,y)$ = local lubricant film pressure, Pa

Downloaded from http://asmedigitalcollection.asme.org/tribology/article-pdf/143/2/021801/6555147/trib_143_2_021801.pdf by Bart Raeymaekers on 25 August 2020

$P(X,Y)$ = non-dimensional local lubricant film pressure, p/p_0
$U_{avg}(X,Y)$ = non-dimensional local average lubricant film velocity
x, y = Cartesian coordinates, m
X, Y = non-dimensional Cartesian coordinates, x/r_p, y/r_p
δ = non-dimensional nominal bearing surface separation, $c/2r_p$
ϵ = texture aspect ratio, $h_p/2r_p$
ϵ_{opt} = optimum texture aspect ratio
λ = flow factor, $3\mu U/2r_p p_0$
μ = dynamic viscosity, Pa·s
ν = Poisson's ratio
σ = Cauchy stress tensor

References

[1] Sloan, M., Premkumar, A., and Sheth, N. P., 2018, "Projected Volume of Primary Total Joint Arthroplasty in the U.S., 2014 to 2030," J. Bone Jt. Surg. Am., **100**(17), pp. 1455–1460.
[2] Foran, J. R. H., 2015, "Total Hip Replacement," Am. Acad. Orthop. Surg, https://orthoinfo.aaos.org/en/treatment/total-hip-replacement, Accessed May 21, 2019.
[3] Heckmann, N. D., Sivasundaram, L., Stefl, M. D., Kang, H. P., Basler, E. T., and Lieberman, J. R., 2018, "Total Hip Arthroplasty Bearing Surface Trends in the United States From 2007 to 2014: The Rise of Ceramic on Polyethylene," J. Arthroplasty, **33**(6), pp. 1757–1763.
[4] Evans, J. T., Evans, J. P., Walker, R. W., Blom, A. W., Whitehouse, M. R., and Sayers, A., 2019, "How Long Does a Hip Replacement Last? A Systematic Review and Meta-Analysis of Case Series and National Registry Reports With More Than 15 Years of Follow-Up," Lancet, **393**(10172), pp. 647–654.
[5] Clohisy, J. C., Calvert, G., Tull, F., McDonald, D., and Maloney, W. J., 2004, "Reasons for Revision Hip Surgery: A Retrospective Review," Clin. Orthop. Relat. Res., **429**, pp. 188–192.
[6] Liu, A., Richards, L., Bladen, C. L., Ingham, E., Fisher, J., and Tipper, J. L., 2015, "The Biological Response to Nanometre-Sized Polymer Particles," Acta Biomater., **23**, pp. 38–51.
[7] Ravi, B., Croxford, R., Reichmann, W. M., Losina, E., Katz, J. N., and Hawker, G. A., 2012, "The Changing Demographics of Total Joint Arthroplasty Recipients in the United States and Ontario From 2001 to 2007," Best Pract. Res. Clin. Rheumatol., **26**(5), pp. 637–647.
[8] Laurent, M. P., Johnson, T. S., Crowninshield, R. D., Blanchard, C. R., Bhambri, S. K., and Yao, J. Q., 2008, "Characterization of a Highly Cross-Linked Ultrahigh Molecular-Weight Polyethylene in Clinical Use in Total Hip Arthroplasty," J. Arthroplasty, **23**(5), pp. 751–761.
[9] Capello, W. N., D'Antonio, J. A., Ramakrishnan, R., and Naughton, M., 2011, "Continued Improved Wear With an Annealed Highly Cross-Linked Polyethylene," Clin. Orthop. Relat. Res., **469**(3), pp. 825–830.
[10] Yamamoto, K., Tateiwa, T., and Takahashi, Y., 2017, "Vitamin E-Stabilized Highly Crosslinked Polyethylenes: The Role and Effectiveness in Total Hip Arthroplasty," J. Orthop. Sci., **22**(3), pp. 384–390.
[11] Oral, E., Christensen, S. D., Malhi, A. S., Wannomae, K. K., and Muratoglu, O. K., 2006, "Wear Resistance and Mechanical Properties of Highly Cross-Linked, Ultrahigh-Molecular Weight Polyethylene Doped With Vitamin E," J. Arthroplasty, **21**(4), pp. 580–591.
[12] Rahaman, M. N., Yao, A., Bal, B. S., Garino, J. P., and Ries, M. D., 2007, "Ceramics for Prosthetic Hip and Knee Joint Replacement," J. Am. Ceram. Soc., **90**(7), pp. 1965–1988.
[13] Brizuela, M., Garcia-Luis, A., Viviente, J. L., Braceras, I., and Oñate, J. I., 2002, "Tribological Study of Lubricious DLC Biocompatible Coatings," J. Mater. Sci. Mater. Med., **13**(12), pp. 1129–1133.
[14] Choudhury, D., Ay Ching, H., Mamat, A. B., Cizek, J., Abu Osman, N. A., Vrbka, M., Hartl, M., and Krupka, I., 2015, "Fabrication and Characterization of DLC Coated Microdimples on Hip Prosthesis Heads," J. Biomed. Mater. Res. Part B: Appl. Biomater., **103**(5), pp. 1002–1012.
[15] Balagna, C., Faga, M. G., and Spriano, S., 2012, "Tantalum-Based Multilayer Coating on Cobalt Alloys in Total Hip and Knee Replacement," Mater. Sci. Eng. C, **32**(4), pp. 887–895.
[16] Ching, H. A., Choudhury, D., Nine, M. J., and Abu Osman, N. A., 2014, "Effects of Surface Coating on Reducing Friction and Wear of Orthopaedic Implants," Sci. Technol. Adv. Mater., **15**(1), p. 014402.
[17] Ito, H., Kaneda, K., Yuhta, T., Nishimura, I., Yasuda, K., and Matsuno, T., 2000, "Reduction of Polyethylene Wear by Concave Dimples on the Frictional Surface in Artificial Hip Joints," J. Arthroplasty, **15**(3), pp. 332–338.
[18] Sawano, H., Warisawa, S., and Ishihara, S., 2009, "Study on Long Life of Artificial Joints by Investigating Optimal Sliding Surface Geometry for Improvement in Wear Resistance," Precis. Eng., **33**(4), pp. 492–498.
[19] Ibatan, T., Uddin, M. S., and Chowdhury, M. A. K., 2015, "Recent Development on Surface Texturing in Enhancing Tribological Performance of Bearing Sliders," Surf. Coatings Technol., **272**, pp. 102–120.
[20] Gropper, D., Wang, L., and Harvey, T. J., 2016, "Hydrodynamic Lubrication of Textured Surfaces : A Review of Modeling Techniques and Key Findings," Tribol. Int., **94**, pp. 509–529.
[21] Borjali, A., Langhorn, J., Monson, K., and Raeymaekers, B., 2017, "Using a Patterned Microtexture to Reduce Polyethylene Wear in Metal-on-Polyethylene Prosthetic Bearing Couples," Wear, **392–393**, pp. 77–83.
[22] Borjali, A., Monson, K., and Raeymaekers, B., 2018, "Friction Between a Polyethylene Pin and a Microtextured CoCrMo Disc, and Its Correlation to Polyethylene Wear, as a Function of Sliding Velocity and Contact Pressure, in the Context of Metal-on-Polyethylene Prosthetic Hip Implants," Tribol. Int., **127**, pp. 568–574.
[23] Langhorn, J., Borjali, A., Hippensteel, E., Nelson, W., and Raeymaekers, B., 2018, "Microtextured CoCrMo Alloy for Use in Metal-on-Polyethylene Prosthetic Joint Bearings: Multi-directional Wear and Corrosion Measurements," Tribol. Int., **124**, pp. 178–183.
[24] Chyr, A., Qiu, M., Speltz, J. W., Jacobsen, R. L., Sanders, A. P., and Raeymaekers, B., 2014, "A Patterned Microtexture to Reduce Friction and Increase Longevity of Prosthetic Hip Joints," Wear, **315**(1–2), pp. 51–57.
[25] Qiu, M., Chyr, A., Sanders, A. P., and Raeymaekers, B., 2014, "Designing Prosthetic Knee Joints With Bio-Inspired Bearing Surfaces," Tribol. Int., **77**, pp. 106–110.
[26] Wang, M., Zhang, C., and Wang, X., 2017, "The Wear Behavior of Textured Steel Sliding Against Polymers," Materials, **10**(4), p. 330.
[27] López-Cervantes, A., Domínguez-López, I., Barceinas-Sánchez, J. D. O., and García-García, A. L., 2013, "Effects of Surface Texturing on the Performance of Biocompatible UHMWPE as a Bearing Material During In Vitro Lubricated Sliding/Rolling Motion," J. Mech. Behav. Biomed. Mater., **20**, pp. 45–53.
[28] Křupka, I., and Hartl, M., 2007, "The Effect of Surface Texturing on Thin EHD Lubrication Films," Tribol. Int., **40**(7), pp. 1100–1110.
[29] Mourier, L., Mazuyer, D., Ninove, F.-P., and Lubrech, A. A., 2010, "Lubrication Mechanisms With Laser-Surface-Textured Surfaces in Elastohydrodynamic Regime," Proc. Inst. Mech. Eng. Part J.: J. Eng. Tribol., **224**(8), pp. 697–711.
[30] Roy, T., Choudhury, D., Ghosh, S., Bin Mamat, A., and Pingguan-Murphy, B., 2015, "Improved Friction and Wear Performance of Micro Dimpled Ceramic-on-Ceramic Interface for Hip Joint Arthroplasty," Ceram. Int., **41**(1), pp. 681–690.
[31] Zhang, B., Huang, W., and Wang, X., 2012, "Biomimetic Surface Design for Ultrahigh Molecular Weight Polyethylene to Improve the Tribological Properties," Proc. Inst. Mech. Eng. Part J.: J. Eng. Tribol, **226**(8), pp. 705–713.
[32] Cho, M., and Choi, H.-J., 2014, "Optimization of Surface Texturing for Contact Between Steel and Ultrahigh Molecular Weight Polyethylene Under Boundary Lubrication," Tribol. Lett., **56**(3), pp. 409–422.
[33] Zhang, B., Huang, W., Wang, J., and Wang, X., 2013, "Comparison of the Effects of Surface Texture on the Surfaces of Steel and UHMWPE," Tribol. Int., **65**, pp. 138–145.
[34] Choudhury, D., Rebenda, D., Sasaki, S., Hekrle, P., Vrbka, M., and Zou, M., 2018, "Enhanced Lubricant Film Formation Through Micro-Dimpled Hard-on-Hard Artificial Hip Joint: An In-Situ Observation of Dimple Shape Effects," J. Mech. Behav. Biomed. Mater., **81**, pp. 120–129.
[35] Qiu, Y., and Khonsari, M. M., 2011, "Experimental Investigation of Tribological Performance of Laser Textured Stainless Steel Rings," Tribol. Int., **44**(5), pp. 635–644.
[36] Wang, W., Huang, Z., Shen, D., Kong, L., and Li, S., 2013, "The Effect of Triangle-Shaped Surface Textures on the Performance of the Lubricated Point-Contacts," ASME J. Tribol., **135**(2), p. 021503.
[37] Choudhury, D., Vrbka, M., Mamat, A. B., Stavness, I., Roy, C. K., Mootanah, R., and Krupka, I., 2017, "The Impact of Surface and Geometry on Coefficient of Friction of Artificial Hip Joints," J. Mech. Behav. Biomed. Mater., **72**, pp. 192–199.
[38] Zenebe Segu, D., and Hwang, P., 2015, "Friction Control by Multi-shape Textured Surface Under Pin-on-Disc Test," Tribol. Int, **91**, pp. 111–117.
[39] Henry, Y., Bouyer, J., and Fillon, M., 2015, "An Experimental Analysis of the Hydrodynamic Contribution of Textured Thrust Bearings During Steady-State Operation: A Comparison With the Untextured Parallel Surface Configuration," Proc. Inst. Mech. Eng. Part J.: J. Eng. Tribol., **229**(4), pp. 362–375.
[40] Meng, X., and Khonsari, M. M., 2017, "On the Effect of Viscosity Wedge in Micro-Textured Parallel Surfaces," Tribol. Int., **107**(November 2016), pp. 116–124.
[41] Rahmani, R., Shirvani, A., and Shirvani, H., 2007, "Optimization of Partially Textured Parallel Thrust Bearings With Square-Shaped Micro-Dimples," Tribol. Trans., **50**(3), pp. 401–406.
[42] Han, J., Fang, L., Sun, J., and Ge, S., 2010, "Hydrodynamic Lubrication of Microdimple Textured Surface Using Three-Dimensional CFD," Tribol. Trans., **53**(6), pp. 860–870.
[43] Zhang, Y. L., Zhang, X. G., and Matsoukas, G., 2015, "Numerical Study of Surface Texturing for Improving Tribological Properties of Ultra-High Molecular Weight Polyethylene," Biosurf. Biotribol., **1**(4), pp. 270–277.
[44] Dowson, D., 1995, "Elastohydrodynamic and Micro-elastohydrodynamic Lubrication," Wear, **190**(2), pp. 125–138.
[45] Basri, H., Syahrom, A., Ramadhoni, T. S., Prakoso, A. T., Ammarullah, M. I., and Vincent, 2019, "The Analysis of the Dimple Arrangement of the Artificial Hip Joint to the Performance of Lubrication," IOP Conf. Ser. Mater. Sci. Eng., **620**(1), p. 012116.
[46] Gao, L., Yang, P., Dymond, I., Fisher, J., and Jin, Z., 2010, "Effect of Surface Texturing on the Elastohydrodynamic Lubrication Analysis of Metal-on-Metal Hip Implants," Tribol. Int., **43**(10), pp. 1851–1860.
[47] Shinkarenko, A., Kligerman, Y., and Etsion, I., 2009, "The Effect of Surface Texturing in Soft Elasto-Hydrodynamic Lubrication," Tribol. Int., **42**(2), pp. 284–292.
[48] Allen, Q., and Raeymaekers, B., 2020, "Maximizing the Lubricant Film Thickness Between a Rigid Microtextured and a Smooth Deformable Surface in Relative Motion, Using a Soft Elasto-Hydrodynamic Lubrication Model," ASME J. Tribol., **142**(7), p. 071802.

Downloaded from http://asmedigitalcollection.asme.org/tribology/article-pdf/143/2/021801/6555147/trib_143_2_021801.pdf by Bart Raeymaekers on 25 August 2020

[49] Yu, H., Wang, X., and Zhou, F., 2010, "Geometric Shape Effects of Surface Texture on the Generation of Hydrodynamic Pressure Between Conformal Contacting Surfaces," Tribol. Lett., **37**(2), pp. 123–130.
[50] Shen, C., and Khonsari, M. M., 2015, "Numerical Optimization of Texture Shape for Parallel Surfaces Under Unidirectional and Bidirectional Sliding," Tribol. Int., **82**(Part A), pp. 1–11.
[51] Zhang, H., Hua, M., Dong, G. Z., Zhang, D. Y., Chen, W. J., and Dong, G. N., 2017, "Optimization of Texture Shape Based on Genetic Algorithm Under Unidirectional Sliding," Tribol. Int., **115**, pp. 222–232.
[52] Zhang, H., Hua, M., Dong, G. N., Zhang, D. Y., and Chin, K. S., 2016, "A Mixed Lubrication Model for Studying Tribological Behaviors of Surface Texturing," Tribol. Int., **93**, pp. 583–592.
[53] Su, B., Huang, L., Huang, W., and Wang, X., 2017, "The Load Carrying Capacity of Textured Sliding Bearings With Elastic Deformation," Tribol. Int., **109**, pp. 86–96.
[54] Wang, X., Wang, J., Zhang, B., and Huang, W., 2015, "Design Principles for the Area Density of Dimple Patterns," Proc. Inst. Mech. Eng. Part J.: J. Eng. Tribol., **229**(4), pp. 538–546.
[55] Shen, C., and Khonsari, M. M., 2013, "Effect of Dimple's Internal Structure on Hydrodynamic Lubrication," Tribol. Lett., **52**(3), pp. 415–430.
[56] Lu, P., Wood, R. J. K., Gee, M. G., Wang, L., and Pfleging, W., 2017, "The Use of Anisotropic Texturing for Control of Directional Friction," Tribol. Int., **113**, pp. 169–181.
[57] Nanbu, T., Ren, N., Yasuda, Y., Zhu, D., and Wang, Q. J., 2008, "Micro-textures in Concentrated Conformal-Contact Lubrication: Effects of Texture Bottom Shape and Surface Relative Motion," Tribol. Lett., **29**(3), pp. 241–252.
[58] Uddin, M. S., Ibatan, T., and Shankar, S., 2017, "Influence of Surface Texture Shape, Geometry and Orientation on Hydrodynamic Lubrication Performance of Plane-to-Plane Slider Surfaces," Lubr. Sci., **29**(3), pp. 153–181.
[59] Sahlin, F., Glavatskih, S. B., Almqvist, T., and Larsson, R., 2005, "Two-Dimensional CFD-Analysis of Micro-patterned Surfaces in Hydrodynamic Lubrication," ASME J. Tribol., **127**(1), pp. 96–102.
[60] Wang, W., He, Y., Zhao, J., Li, Y., and Luo, J., 2017, "Numerical Optimization of the Groove Texture Bottom Profile for Thrust Bearings," Tribol. Int., **109**, pp. 69–77.
[61] Ford, W., 2015, *Numerical Linear Algebra with Applications Using MATLAB*, Elsevier Inc, San Francisco, CA.
[62] Bergström, J. S., Kurtz, S. M., Rimnac, C. M., and Edidin, A. A., 2002, "Constitutive Modeling of Ultra-High Molecular Weight Polyethylene Under Large-Deformation and Cyclic Loading Conditions," Biomaterials, **23**(11), pp. 2329–2343.
[63] Shinkarenko, A., Kligerman, Y., and Etsion, I., 2009, "The Validity of Linear Elasticity in Analyzing Surface Texturing Effect for Elastohydrodynamic Lubrication," J. Tribol., **131**(2), pp. 021503–1–021503–7.
[64] Saikko, V., 2006, "Effect of Contact Pressure on Wear and Friction of Ultra-High Molecular Weight Polyethylene in Multidirectional Sliding," Proc. Inst. Mech. Eng. Part: H Eng. Med, **220**(7), pp. 723–731.
[65] Brizmer, V., Kligerman, Y., and Etsion, I., 2003, "A Laser Surface Textured Parallel Thrust Bearing," Tribol. Trans., **46**(3), pp. 397–403.
[66] Pinkus, O., and Sternlicht, B., 1961, *Theory of Hydrodynamic Lubrication*, McGraw-Hill Book Company, New York.
[67] Codrignani, A., Frohnapfel, B., Magagnato, F., Schreiber, P., Schneider, J., and Gumbsch, P., 2018, "Numerical and Experimental Investigation of Texture Shape and Position in the Macroscopic Contact," Tribol. Int., **122**, pp. 46–57.
[68] Rahmani, R., and Rahnejat, H., 2018, "Enhanced Performance of Optimised Partially Textured Load Bearing Surfaces," Tribol. Int., **117**, pp. 272–282.
[69] Vlădescu, S. C., Olver, A. V., Pegg, I. G., and Reddyhoff, T., 2016, "Combined Friction and Wear Reduction in a Reciprocating Contact Through Laser Surface Texturing," Wear, **358–359**, pp. 51–61.
[70] Etsion, I., 2005, "State of the Art in Laser Surface Texturing," ASME J. Tribol., **127**(1), pp. 248–253.
[71] Dong, Y., Svoboda, P., Vrbka, M., Kostal, D., Urban, F., Cizek, J., Roupcova, P., Dong, H., Krupka, I., and Hartl, M., 2016, "Towards Near-Permanent CoCrMo Prosthesis Surface by Combining Micro-texturing and Low Temperature Plasma Carburising," J. Mech. Behav. Biomed. Mater., **55**, pp. 215–227.
[72] Xu, Y., Zheng, Q., Abuflaha, R., Olson, D., Furlong, O., You, T., Zhang, Q., Hu, X., and Tysoe, W. T., 2019, "Influence of Dimple Shape on Tribofilm Formation and Tribological Properties of Textured Surfaces Under Full and Starved Lubrication," Tribol. Int., **136**, pp. 267–275.
[73] 2011, "Implants for Surgery-Partial and Total Hip Joint Prostheses-Part 2: Articulating Surfaces Made of Metallic, Ceramic and Plastic Materials," ISO 7206-2, **E**, p. 6.
[74] Mattei, L., Di Puccio, F., Piccigallo, B., and Ciulli, E., 2011, "Lubrication and Wear Modelling of Artificial Hip Joints: A Review," Tribol. Int., **44**(5), pp. 532–549.
[75] Gao, L., Dowson, D., and Hewson, R. W., 2016, "A Numerical Study of Non-Newtonian Transient Elastohydrodynamic Lubrication of Metal-on-Metal Hip Prostheses," Tribol. Int., **93**(Part B), pp. 486–494.
[76] Ghosh, S., Choudhury, D., Roy, T., Moradi, A., Masjuki, H. H., and Pingguan-Murphy, B., 2015, "Tribological Performance of the Biological Components of Synovial Fluid in Artificial Joint Implants," Sci. Technol. Adv. Mater., **16**(4), p. 045002. (12 pages).
[77] Nečas, D., Vrbka, M., Galandakova, A., Křupka, I., and Hartl, M., 2019, "On the Observation of Lubrication Mechanisms Within Hip Joint Replacements. Part I: Hard-on-Soft Bearing Pairs," J. Mech. Behav. Biomed. Mater., **89**, pp. 237–248.
[78] Qiu, Y., and Khonsari, M. M., 2009, "On the Prediction of Cavitation in Dimples Using a Mass-Conservative Algorithm," ASME J. Tribol., **131**(4), p. 041702.
[79] Ausas, R., Ragot, P., Leiva, J., Jai, M., Bayada, G., and Buscaglia, G. C., 2007, "The Impact of the Cavitation Model in the Analysis of Microtextured Lubricated Journal Bearings," ASME J. Tribol., **129**(4), pp. 868–875.
[80] Dobrica, M. B., Fillon, M., Pascovici, M. D., and Cicone, T., 2010, "Optimizing Surface Texture for Hydrodynamic Lubricated Contacts Using a Mass-Conserving Numerical Approach," Proc. Inst. Mech. Eng. Part J.: J. Eng. Tribol., **224**(8), pp. 737–750.

Downloaded from http://asmedigitalcollection.asme.org/tribology/article-pdf/143/2/021801/6555147/trib_143_2_021801.pdf by Bart Raeymaekers on 25 August 2020